中國機械工程學刊第四十三卷第五期第 379~388 頁(民國一百一十一年)
Journal of the Chinese Society of Mechanical Engineers, Vol.43, No.5, pp.379~388 (2022)

# Enhancing System Efficiency of Valveless Micropumps by Using Bio-inspired Chambers

Hsin-Yi Lai [*]and Jing-Hao Kang [**]

**Keywords**：*valveless micropump, enhanced bio-inspired chamber, fluid-solid coupling system*

## ABSTRACT

In order to expand the back pressure and increase the net flow rate of the micropump, so as to achieve the purpose of being applicable to high-performance industrial and medical micro-systems, a complete set of theoretical and numerical modeling methods are proposed in this paper to design for enhancing system efficiency of a bio-inspired chamber for the valveless micropump. To ensure the design goal can be achieved, a two-way fluid-solid coupling interface system (FSIS) is adopted for design analysis of the bio-inspired chamber structure. The design and numerical simulation process indicates that when the peak voltage is of 100 V and working frequency is at 40 Hz, maximum net flow rate of the bio-inspired micropump is 1.89 ml/min and maximum back pressure is 720 PA (or 5.4 mmHg), which are better than that of the conventional micropump with circular geometry. Also, the net flow rate of the bio-inspired system is 44% higher than that of the conventional micropump. The results also reveal that the internal flow state of the bio-inspired valveless micropump possesses a significant impact on the increase of the natural frequency of the system. Since the system resonance frequency thus induced is much higher, the net flow rate of the bio-inspired micro-pump is thus effectively increased. By comparing with the measured data of the conventional circular valveless micropump system, it is proved that the bio-inspired chamber design proposed in this paper is highly feasible.

## INTRODUCTION

Microelectromechanical actuators have been widely used in various industrial systems in recent years, and among them precision micropumps in experimental chips have been shown to have the greatest development potential and economic benefits [1–4]. For valveless micropumps, Stemme et al. [5] first produced a microfluidic pump using brass and valveless structure in 1993. The geometric parameters of this pump include a 19 mm micro-vibration cavity diameter, 16 mm piezoelectric sheet diameter, 16 ml/min maximum flow rate, and 19.6 kPa maximum backpressure. Utilizing the characteristics of inverse voltage for piezoelectric materials and a valveless structural design, this pump was found to possess many advantages, including good biocompatibility and a simple and reliable structure. In the historical development of micropump systems, piezoelectric micropumps was considered as the most promising microfluidic delivery devices. However, their backflow effect, high input voltage, and low energy conversion rate hinder practical industrial applications.

In 2004, Laser et al. [6] discussed various developments in micropumps over the past 25 years. They indicated that the reciprocating dynamic mechanism is the main effective working process of the micropump system. In recent years, various principles and driving mechanisms were proposed and widely used in micropumps, including electromagnetic, electrostatic, shape memory, and piezoelectric mechanisms. Among these, piezo-electric (PZT) actuators provide characteristics of high driving force, responsive frequency conversion, and high deflection to satisfy the microfluidic requirements of micropumps. In addition, valve damage can be avoided through the nozzle diffusion element and chamber structure redesign, thereby increasing the reliability of the overall system.

Gerlach et al. [8] and Koch et al. [9] performed experimental measurements of the parameters of micropump in 1995 and 1998, respectively. Their research results indicated that micropumps reach the maximum mass flow rate as the AC frequency is close to the natural frequency of the system. However, when the Koch team compared the new and conventional micropump designs, they found that new design of micropumps has increased operating efficiency by approximately three to six times. Afrasiab et al. [10] verified different waveforms

---

*Paper Received June, 2022. Revised Augus,t 2022. Accepted August, 2022. Author for Corresponence: Jing-Hao Kang*

[*] *Professor, Department of Mechanical Engineering, National Cheng Kung University, Tainan, Taiwan, ROC.*

[**] *Ph.D. candidate, Department of Mechanical Engineering, National Cheng Kung University, Tainan, Taiwan, ROC.*

generated by symmetrical obstacles and walls using a three-dimensional finite element method in 2011. The results showed that the waveforms generated from different wall shapes could increase the flow rate of a micropump by a factor of seven.

Since micropumps are usually required to be processed by several microelectromechanical processes, and each processing experiment inevitably requires high cost and labor, numerical fluid simulation is thus gradually become a major part in the new design process. In 2000, Olsson et al. [11] stated that there is a close relationship between the angle of the microchannels in micropumps and the Reynolds number of a fluid, but the length of the channels plays no significant effect on the flow rate. In 2014, Xu et al. [12] proved through a numerical simulation that sawtooth channels can increase the flow rate of a micropump by 25%. Dich et al. [13] simulated the dynamic behavior of micropumps via CFD, and the backpressure range of micropumps were analyzed and discussed in 2015. Singh et al. [14] proposed a water drop-shaped PDMS micropump in 2015. Their pump employed a single-use membrane pump chamber, with the shape of the chamber with the outlet zone modified by a 120° cone angle. Their valveless micropump was found to be 28% more efficient than the conventional one. These results indicated that the net flow rate of a micropump can be significantly affected by the voltage frequency, microchannel angle, chamber height, microchannel length, channel width, and membrane thickness. In 2021, Lai et al. [15] defined the pump efficiency index of a micropump through numerical analysis method, and proposed a new chamber enhancement design based on streamline distribution. The results indicate that the enhancement of chamber design can result in four circulation regions, which in turn enhance the internal forward flow velocity to slow down the backflow effect.

In micropump systems, the flow rate and the backpressure range are two major performance indicators. Many studies have proposed the enhanced designs to increase the flow rate by approximately 20% to 50%. These study have focused on the effect of nozzle/diffuser and bio-inspired chambers on the flow rate.

A bio-inspired design was made by improving the outlet zone diameter, nozzle angle, diffuser angle, and offset parameters, and the effect of these parameters on the system's flow rate was investigated. Bio-inspired design parameters were presented based on the research results and compared with the flow rate and backpressure range of a conventional design. It is expected that the overall efficiency of the system will be greatly improved, making this enhanced micropump system widely applicable to the engineering and healthcare industries.

In this study, a novel micropumps is proposed and designed by employing piezoelectric actuators with a bio-inspired chamber. The new system possesses many advantages including a simple shape, stability, high durability, and high flow rate. It is expected to be used in industrial microfluidic equipment, microbiochips, and other human engineering systems that require efficient liquid delivery, such as micromechanical lubrication for power and drug delivery. For safety considerations, the requirements for the proposed bio-inspired valveless micropump system were restricted to the following given environment conditions, such as a working pressure in the range of 0–1330 Pa (or 10 mmHg) and a natural system frequency of 40–70 Hz. In addition, the micropump system must meet the requirements of durability and flow rate stability. The durability of the micropump should be able to lower the costs of system disassembly and repair, whereas the flow rate stability should be able to enhance the reliability for liquid delivery and feeding.

## Modelling Methodology

The two processes that occur during the complete working cycle of a valveless micropump are generally called the intake and outlet processes, as shown in Figure 1. During the intake process, the volume of the chamber increased, and the fluid passed through the diffuser from the inlet before flowing into the chamber through the nozzle. When the fluid flowed through the nozzle, the cross-sectional area decreased and the flow velocity increased, resulting in a higher flow resistance. However, when the fluid flows through the diffuser, the cross-sectional area increases and the flow velocity decreases, resulting in a lower flow resistance. Therefore, the volume flow through the diffuser via the inlet was generally greater. Similarly, in the outlet process, the volume of the chamber decreased and the liquid was discharged, while the original nozzle became a diffuser owing to the opposite flow direction, and the diffuser became a nozzle. Therefore, when the fluid is discharged, more liquid will flow out of the outlet than liquid flowing in from the inlet, and the net flow rate can be obtained at the outlet after one cycle.

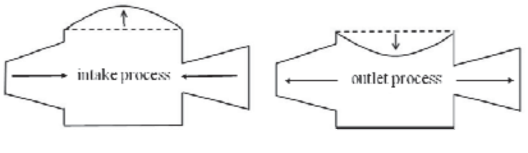

Fig. 1 Operating sequences of the valveless pump

### System Dynamic Equations

The deformation generated by the inverse voltage effect of the piezoelectric materials used in this study drove the elastic membrane. According to the theory of elasticity [16], the governing equations of an elastic structure consist of 15 equations, and 15 unknown coefficients can be obtained through the force balance, strain-displacement, and stress-strain relationships. In this study, it is assumed that the deflection of the elastic membrane is relatively minor compared to the characteristic length. Therefore, the fluid-solid interface can be defined as a membrane, and the governing equation for membrane deflection can be expressed as

$$\frac{Eh^3}{12(1-v^2)}\nabla^4 w + \rho_m t\frac{\partial^2 w}{\partial t^2} = f_a - p \tag{1}$$

where $E$, $\rho$, $v$, $t$ represent the Young's modulus, density, Poisson's ratio, and height of the membrane respectively, and $f_a$ and $P$ are the force and hydraulic load of the membrane given by the piezoelectric actuator, respectively. The structural deformation of the piezoelectric actuator and the membrane due to electric-solid coupling can be expressed as

$$\gamma_{ij} = s_{ijks}\sigma_{ks} + d_{kij}E_k \tag{2}$$

$$D_i = d_{ijk}\sigma_{jk} + \varepsilon_{ik}{}^T E_k \tag{3}$$

where $E_k$ is the electric field, $\sigma_{ks}$ the stress field (N/m$^2$), $D_i$ the electric displacement (C m$_{-2}$), $s_{ijks}$ the flexibility matrix (m$^2$/N), $\varepsilon_{ik}^T$ the dielectric constant (F/m), and $d_{ijk}$ the piezoelectric strain constant (m/V).

The fluid model proposed in this study does not consider the effect of temperature and gravitational fields on the flow field, which can therefore be assumed to be an incompressible flow. According to the conservation of mass and momentum, the flow field can be expressed as follows using the three-dimensional Navier–Stokes equations:

$$\nabla \cdot V = 0 \tag{4}$$

$$\frac{d}{dt}(\rho V) = -\nabla P + \mu\nabla^2 V \tag{5}$$

where $\rho$ and $\mu$ are definite values that represent the density and viscosity coefficients of the fluid, respectively. $V$ is the velocity vector of the flow field system.

## Modeling of Conventional Cylindrical Valveless Micropumps

To build up the numerical model of a piezoelectric-driven valveless micropump, we considered the electric-solid coupling characteristics of the piezoelectric actuator and mapped the driving membrane displacement data to the elastic membrane via the fluid-solid coupling system (FSCS) as the boundary condition for a fluid numerical analysis in order to perform iterative calculations of the two-way fluid-solid coupling. As the elastic membrane deflection in the piezoelectric actuator is much smaller than the characteristic length, the governing equation for the membrane is given by Equation (1). The governing equation for the fluid calculation is given in equations (4-5), where the pressure $P$ and velocity field $u_i$ can be obtained according to the geometric shape and reasonable boundary conditions of the valveless micropump proposed in this paper.

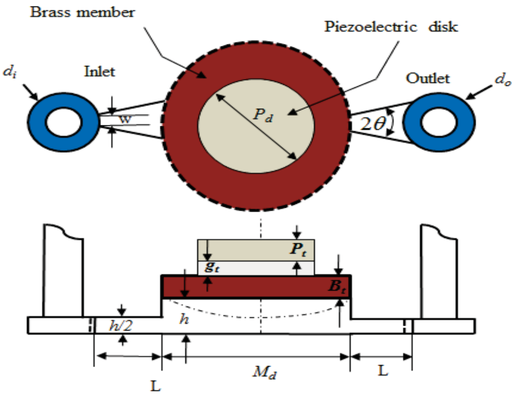

Fig. 2 Geometric parameters used in a piezoelectric valveless micropump

Figure 2 shows a schematic of the conventional piezoelectric valveless micropump structure design. The blue areas in the figure represent the micropump inlet and outlet zones. The chamber diameter and height of the micropump were set to $M_d$ and $h$, respectively. We covered the boundary on the chamber with an elastic membrane, adhered the piezoelectric material to the elastic membrane with epoxy, and finally connected the plastic tubes to the inlet and outlet zones of the micropump. To prevent the micropump from flowing back into the inlet and outlet zones, the length and diameter of the two plastic tubes were set as 10 cm and 1 mm, respectively. The dimensions of the conventional micropump used in this study were as follows: opening angle, $2\theta = 10^\circ$, channel length, $L = 9$ mm, narrowest point in the channel, $w = 0.5$ mm, inlet pipe diameter, $d_i = 3$mm, outlet pipe diameter, $d_o = 3$ mm, and chamber height, $h = 2$ mm . The materials and dimensions of the piezoelectric actuator, elastic membrane, epoxy, and working fluid (water) are presented in Table 1.

### (i) Boundary conditions

Zero-displacement boundary conditions are given for the surroundings of the elastic membrane, while the contact surfaces between the elastic membrane, epoxy, and piezoelectric actuator are all bonded. For the upper and lower surface layers of the piezoelectric actuator, sinusoidal voltage and zero potential are given, respectively. The sinusoidal voltage can be expressed as

$$V = 100 \times \sin(2 \times \pi \times f \times time) \tag{6}$$

For the fluid, constant pressure boundary conditions are given at the contact surface between the two water pipes and air, and a fluid-solid interface is provided, by which the deflection behavior of the structural domain is acceptable. The remaining boundaries were set as nonslip walls.

Table 1 Geometric and material parameters used in a PZT-4 piezoelectric actuator

| Material used | Size | Parameters | Data |
|---|---|---|---|
| brass | thickness $B_t$=180μm<br>diameter: $M_d$=25mm | modulus $E_b$ (Pa)<br>viscosity $\upsilon_b$<br>density (kg m$^{-3}$) | $1.1\times10^{11}$<br>0.32<br>8400 |
| epoxy | thickness $G_t$=100μm<br>diameter $G_d$=20mm | modulus $E_g$ (Pa)<br>viscosity $\upsilon_g$<br>density (kg m$^{-3}$) | $9.79\times10^{8}$<br>0.3<br>1500 |
| PZT 4A<br>[17-18] | thickness $P_t$=200μm<br>diameter $P_d$=20mm | piezoelectricity (C m$^{-2}$) | $\begin{bmatrix} 0 & 0 & -5.2 \\ 0 & 0 & -5.2 \\ 0 & 0 & 15.1 \\ 0 & 0 & 0 \\ 12.7 & 0 & 0 \\ 0 & 12.7 & 0 \end{bmatrix}$ |
| | | permittivity (F m$^{-1}$) | $\begin{bmatrix} 6.45 & 0 & 0 \\ 0 & 6.45 & 0 \\ 0 & 0 & 5.61 \end{bmatrix}\times10^{-9}$ |
| | | elasticity matrix (N m$^{-2}$) | $\begin{bmatrix} 13.9 & 7.78 & 7.43 & 0 & 0 & 0 \\ 7.78 & 13.9 & 7.43 & 0 & 0 & 0 \\ 7.43 & 7.43 & 11.9 & 0 & 0 & 0 \\ 0 & 0 & 0 & 3.06 & 0 & 0 \\ 0 & 0 & 0 & 0 & 2.56 & 0 \\ 0 & 0 & 0 & 0 & 0 & 2.56 \end{bmatrix}$ |
| | | density (kg m$^{-3}$) | 7500 |

### (ii) Converged mesh and element types

Figure 3 shows the optimal mesh for the numerical model used in this study, which can be divided into body size and number of edge divisions. Table 2 lists the best convergence results and division parameters. When the numerical models shown in Figure 3(a) and Figure 3(b) are used for the two-way fluid-solid coupling calculation, 15,000 and 140,000 elements are used for the structural domain and flow domains, respectively, and the deflection error and net flow rate error of the membrane are approximately 1%. Using two-way fluid-solid coupling calculation, additional meshes can lead to significantly longer calculation times without improvements in accuracy. Eight cycles were used throughout the calculation process, and each cycle took approximately 12–18 hours.

### (iii) Relaxation factor of the fluid-solid coupling system (FSCS)

Based on the model presented above, a two-way fluid-structure coupling numerical procedure was used to construct the valveless micropump model used for the system simulation. However, to maintain the deformation data for the FSI interface stable during the iteration process, the calculation variables were adjusted using the relaxation factor in the computation step. The generalized iterative equation used in this process is given as

$$U_{i+1} = U_i + r_{i+1}\Delta U_{i+1} \qquad (7)$$

$$\Delta U_{i+1} = \hat{U}_{i+1} - U_i \qquad (8)$$

where $U$ represents the variables associated with a given relaxation factor, $r$ is the relaxation factor, $\hat{U}$ represents the estimated parameters without using the relaxation factor, and $i$ is the number of iterations per unit time-step. Generally, a smaller relaxation factor improves the stability of the fluid-structure coupling computation. However, the required computational time and the associated costs increase. A relaxation factor of 0.75 was generally adopted for our simulation to make it possible to achieve stable numerical results.

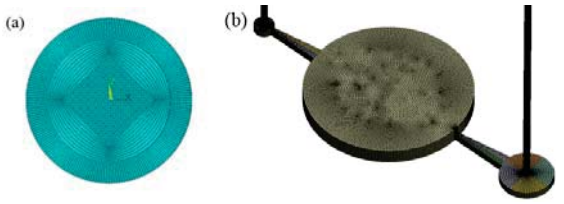

Fig. 3 Converged model: (a) piezoelectric actuator, (b) flows in the micropump

Table 2 Converged parameters used in discretized mesh models

| | mesh type | mesh size |
|---|---|---|
| piezoelectric actuator | body mesh | body size: $2.5\times10^{-4}$<br>thickness divisions: 3 |
| pump chamber | body mesh | body size: $3.2\times10^{-4}$<br>thickness divisions: 10 |
| inlet/outlet opening | number of edge divisions | length: 50<br>width: 6<br>thickness: 5 |
| outlet/inlet zone | number of edge divisions | diameter: 64<br>thickness: 5 |
| outlet/inlet flow pipe | number of edge divisions | length: 200<br>diameter: 64 |

## Innovative Design of Bio-inspired Chambers

As presented above, we can now confirm that the numerical model has a high degree of reliability to the real model. The modified chamber outlet shape of the bio-inspired valveless micropump will then proposed based on the measurements of the actual shape of a moving stingray to design for enhancement of the flow characteristics and overall system efficiency. The design procedures are given as (1) curve fitting of polynomial equations is carried out based on the given measured data; (2) the resulting stingray shape and modified chamber shape of the bio-inspired micropump chamber is obtained and expressed as

stingray: $$y = 5.37x^4 - 14.38x^3 + 14.94x^2 - 6.50x + 0.50 \qquad (9)$$

bio-inspired chamber:

$$y = 2.42x^4 - 5.08x^3 + 4.58x^2 - 1.72x - 0.29 \qquad (10)$$

and (3) plugging eleven data points in the range of into Equations (9-10) to optimize the parameters in the equation to allow RMSE (root mean squared errors) between them being minimized in the sense of minimal nonliner least squared errors.

Figures 4 and 5 show the fitting curves of the bio-inspired chamber shape and that of the moving stingray, as well as the design concepts and parameter relations. As shown in the figures, the bio-inspired design curve can form an offset arc through offset *d'*, this offset arc and the outer circle of the conventional chamber intersect at two points, the offset arc connected between the two points is the curve of the bio-inspired chamber outlet generated from offset *d'*. It is worth noting that when offset *d'* is 0.015 m, the bio-inspired design curve is highly consistent with the shape curve of a stingray.

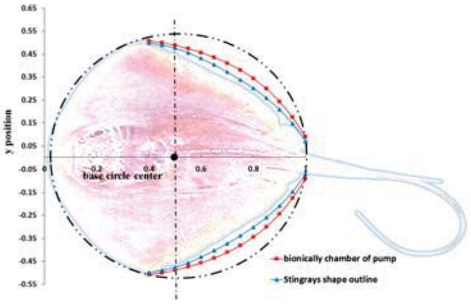

Fig. 4 Shape design for the bio-inspired chamber

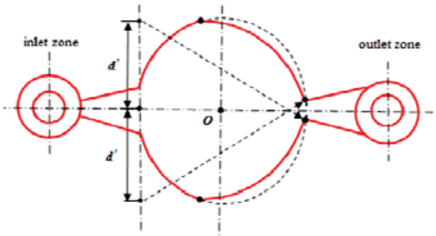

Fig. 5 Bio-inspired chamber design via an offset of *d'*

## Design Procedure and Numerical Model of the Bio-inspired Chamber

Figure 6 shows the design steps for the bio-inspired chamber proposed in this study, where the smooth shape can be engineered through offset arcs. The improvement steps included the following: Offset the centerline of the inlet of the circular chamber upward and downward by $d'$. The two points after the offset were used as the center of the circle. The distance from the center of the circle to the upper and lower points of the diffuser throat is used as the radius to establish two smooth correction arcs that change with offset $d'$, and these two correction arcs are used as the shape for the curve of the micropump chamber outlet.

For the geometric shape of a conventional micropump chamber, parametric equations can be expressed as

$$x = r\cos\theta \tag{11}$$

$$y = r\sin\theta \tag{12}$$

Since the chamber diameter of the conventional micropump $M_d$ is 0.025 m, the geometric shape of the chamber is a circular body with the center of the circle at (0, 0) with a radius of 0.0125 m. As for the final shape of the bio-inspired chamber design proposed in this study, as shown in Figure 4, a circle is drawn with point $Q_c$ and offset by *d'*, the above chamber inlet as the center of the circle, where the distance from $Q_c$ to $Q_o$- is the radius. The offset arc of the circle and outer circle of the chamber intersect at $Q_p$. The distance between $Q_o$- and $Q_p$ is the arc length of the outlet wall of the stingray shaped chamber. The parametric equations of the circle can be expressed as

$$x = \sqrt{{M_d}^2 + d'}\cos\theta - \frac{M_d}{2}\text{, where } \theta_1 = tan^{-1}\frac{d'}{M_d} \tag{13}$$

$$y = \sqrt{{M_d}^2 + d'}\sin\theta - d'\text{, where } \theta_2 = tan^{-1}\frac{L_2 + d'}{L_1}. \tag{14}$$

The geometric shape of the chamber is improved according to the correction arcs formed by equations (13-14), where the value of offset $d'$ can be precisely adjusted to obtain a smooth shape closer to the micropump. The effects of smooth arcs in the outlet chamber on the net flow rate are discussed in detail below.

## Modeling Results and Discussion

To ensure an accurate comparison with the experimental results given in the literature, our simulation model explicitly followed the physical structure described by Wang [19]. Figure 7 shows a comparison of the net flow between the two-way fluid-structure coupling numerical simulation and the data given in literature. The results in the figure indicate that the net flow rate and dynamic characteristics of the numerical model at the resonance frequency are consistent with the experimental measurement.

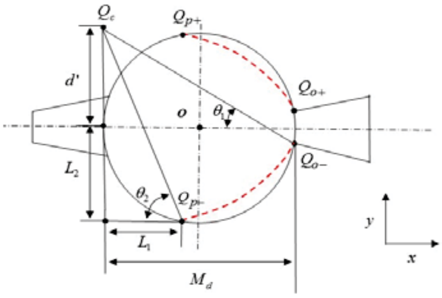

Fig. 6 Design steps of the bio-inspired chamber

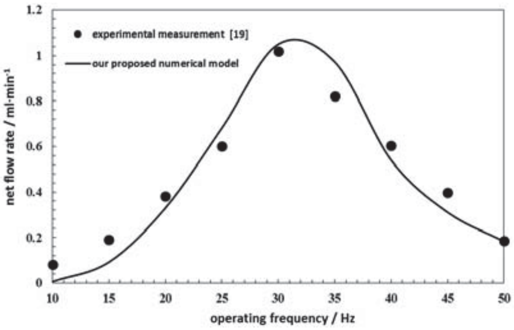

Fig. 7 The numerical model as compared to the experimental measurements [19]

Table 3 lists the net flow performance of the conventional micropump obtained from the simulation data. These results indicate that the numerical model produced a net flow of 1.06 ml/min at 30 Hz. It was found that the maximum error in the net flow rate was approximately 3.8%. This result confirms that the two-way fluid-solid coupling numerical method is reliably accurate. Interestingly, in the simulation process, the system operating frequency was generally greater than that of the system resonant frequency obtained using the measurement data. This is because of the increase in the rate of volume change in the chamber, which slowed down the flow rate by returning to the normal state. Therefore, a longer operational period of 10–16 computational cycles is required.

Table 3 Comparison of the net flow rates

| Operating frequency, Hz | The proposed numerical model | Experimental measurement [19] |
|---|---|---|
| 10 | 0.006 | 0.08 |
| 15 | 0.092 | 0.192 |
| 20 | 0.330 | 0.382 |
| 25 | 0.681 | 0.602 |
| 30 | 1.050 | 1.020 |
| 35 | 0.972 | 0.821 |
| 40 | 0.540 | 0.604 |
| 45 | 0.311 | 0.398 |
| 50 | 0.183 | 0.186 |

## Characterization of Flow Dynamics in Bio-inspired Chambers

In the solid structural domain, the upper surface layer of the piezoelectric material was given a sinusoidal voltage, and the surroundings of the elastic membrane were fixed with zero-displacement boundary conditions. The displacement distribution at the deformation contour of the structural domain and the solid interface is shown in Figure 6. The analytical results indicate that the maximum deflection of the elastic membrane occurs at the center, and the deflection value is approximately 21.7 μm. Figure 8(a) shows the deflection of the fluid-solid interface. This deflection is the result of the positive strain of the piezoelectric material being affected by the difference in potential, causing the elastic membrane with fixed surroundings to bend both upward and downward. As shown in Figure 8(b), when the operating frequency gradually approached the system frequency, the natural mode of the piezoelectric material began to affect the deflection value, where the maximum deflection occurred at 30 Hz. At operating frequency of 35 Hz, because the frequency exceeded the natural frequency of the system, the deflection began to decrease. However, when the deflection began to change accordingly, the system flow rate was affected.

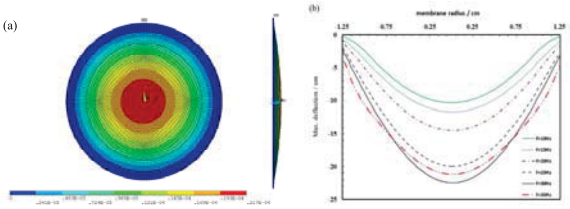

Fig. 8 Dynamic behavior of the elastic membrane
(a) membrane displacement contour,
(b) deflection profile at fluid-solid interface

Figure 9(a) shows the streamline distribution of conventional micropump in the intake/outlet process. Owing to the upward deflection of the elastic membrane, the pressure gradient within the microfluidic channel creates a synthetic jet at the outlet opening to obtain a net flow of the system. Figure 9(b) shows the streamline distribution of bio-inspired micropump in the intake/outlet process. The streamline distribution results show that the bio-inspired chamber design increases the pressure gradient of the fluid flowing forward, resulting in a more concentrated synthetic jet at the outlet. Furthermore, because the pressure drop between the inlet and outlet openings increases, the bio-inspired chamber generates a pair of vortices at the inlet to reduce the backflow at the outlet. This indicates that the potential improvement on diffuser/nozzle effect of the bio-inspired chamber design, thereby increasing the net flow of the micropump.

## Effect of the Divergence Angles on System Net Flow Rate Increment

Figure 10 shows the effect of the inlet/outlet opening divergence angle on the flow rate in the outlet process. As shown in the figure, the highest flow rate was reached when the outlet opening divergence angle was 14° and when the inlet opening divergence angle was 6°. It is worth noting that the system's optimal flow rate was reached when the divergence angles of the two channels were different. The difference between the highest and lowest flow rates was approximately 0.39 ml min-1 for the outlet opening and approximately 0.184 ml min-1 for the inlet opening. Therefore, in the outlet process, the effect of the divergence angle on the flow rate at the outlet opening was greater than that at the inlet opening.

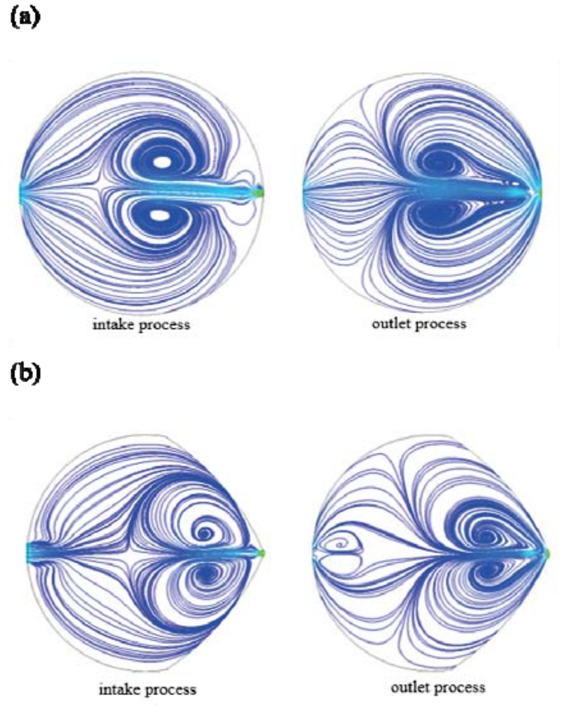

Fig. 9 Streamline distribution in the intake/outlet process: (a) conventional chamber and (b) bio-inspired chamber

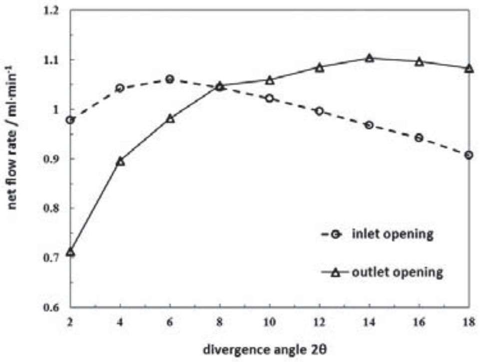

Fig. 10 Effect of divergence angles on system net flow rate increment

## Effect of Channel Length and Throat Width on System Net Flow Rate Increment

Figure 11(a) shows that the maximum flow velocity on the central line of the chamber and the maximum net flow rate of the system are affected by the channel length. When the channel length was 9 mm, the maximum flow velocity along the central line of the chamber was 0.214 m/s. This means that, owing to the low internal eddy velocity, the valveless micropump has an optimal flow rate under such conditions. According to the research results, both short and long channel lengths lower the flow rate because the change in the pressure drop caused by the channel length creates a reverse vortex inside the chamber, hindering the flow velocity of the fluid.

Figure 11(b) shows that, in the outlet process, the maximum flow velocity on the central line of the chamber and the maximum net flow rate of the system are affected by the channel width. In the case of a narrow channel width, the internal eddy velocity increased proportionally. The net flow rate increased as the width was reduced and began to drop sharply when the channel width reaches 0.3 mm, decreasing the efficiency of the micropump. This indicates that the channel width has a significant impact on the increase in the net flow rate. According to the results of the numerical simulation, in the case of a smaller width, a larger vortex was generated inside the chamber owing to the pressure change, which caused the internal fluid to merge and flow to the outlet, creating a merged shooting flow. In the case of a larger channel width, the internal flow was relatively mild and the merged shooting flow was less obvious.

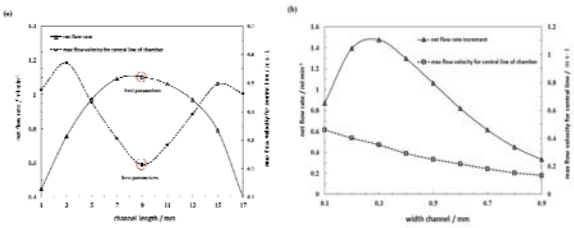

Fig. 11 Effect of inlet/outlet opening sizes on net flow rates and maximum flow velocity along the central line of chamber: (a) lengths, and (b) widths

## Effect of Asymmetric Offset Variable on the Increment of System Net Flow Rate

Figure 12 shows the effect of the offset parameter d’ on the flow rate of the system. As shown in the figure, the relationship between the offset parameter and the system flow rate is not linear, and the optimal flow rate of the bio-inspired design at the outlet reaches 1.88 ml/min when the offset parameter value is approximately 2.5 mm. It is worth noting that, as shown in the enhanced chamber inlet curve in Figure 12, the optimal flow rate of the bio-inspired design at the outlet occurs when the offset parameter value is 0 mm. This net flow rate increment shows a declining trend opposite to the sigmoid results, which means that the flow at the inlet of the smooth shaped design is not suitable for further shape improvement. The same results are shown in the detailed design parameter values for the inlet and outlet of the bio-inspired micropump chamber provided in Table 4.

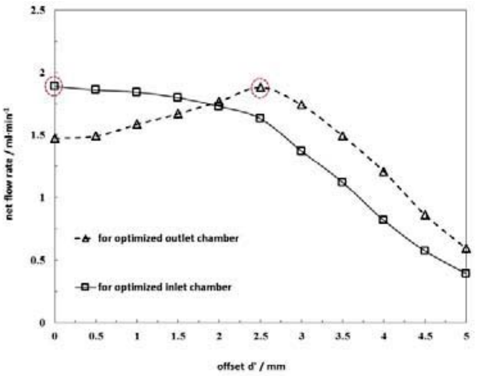

Fig. 12 Effect of asymmetric offset on system net flow rate for both micropump models

Table 4 Design parameters used for the bio-inspired chamber

| Geometric parameters | Dimensions |
|---|---|
| inlet zone diameter | 3 mm |
| outlet zone diameter | 8 mm |
| outlet divergence angle | 14º |
| inlet divergence angle | 6º |
| length of channel | 9 mm |
| throat width in channel | 0.3 mm |
| design of *d'* for the chamber's near outlet area | 2.5 mm |
| design of *d'* for the chamber's near inlet area | 0 mm |

## Effect of operating frequency on System Flow Rate Increment

In a valveless micropump, the interaction between the resonant frequency and operating frequency is important. As mentioned frequently in the literature, the optimal net flow rate is usually achieved when the system is in a resonant state. Figure 13 shows the relationship between the net flow rate of the two different micropump models mentioned in this paper at different operating frequencies. Table 5 shows that the flow rate of the bio-inspired micropump is generally better than that of the conventional micropump. The flow rates of the two designs were almost identical when the operating frequency was lower than 20 Hz. However, the flow rate of the bio-inspired micropump began to increase significantly when the operating frequency exceeded 30 Hz. This is owing to an increase in the resonant frequency of the bio-inspired micropump, causing its optimal operating frequency to increase from 31 Hz to 40 Hz. This also implies that the net flow rate of a micropump at a higher resonant frequency is better than that of a system with a lower resonant frequency.

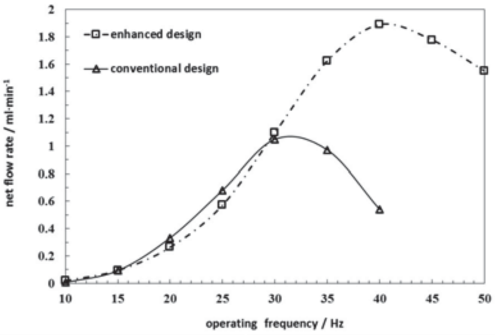

Fig. 13 Effect of operating frequency on system net flow rate for both micropump models

Table 5 Net flow rate increments for both the bio-inspired and conventional chambers

| operating freq. (Hz) | | bio-inspired chamber (ml $min^{-1}$) | conventional chamber (ml $min^{-1}$) |
|---|---|---|---|
| 10 | | 0.019 | 0.006 |
| 15 | | 0.094 | 0.092 |
| 20 | | 0.264 | 0.333 |
| 25 | | 0.573 | 0.681 |
| 30 | | 1.100 | 1.059 |
| 35 | | 1.624 | 0.972 |
| 40 | | 1.890 | 0.54 |
| 45 | | 1.776 | |
| 50 | | 1.550 | |
| | | net flow rate increment | 44 % |

## Effect of backpressure and resonant frequency on system responses

For safety reasons, the driving frequency used by medical devices must be strictly controlled, because even the slightest alternating current transmitted to the human heart can cause fibrillation and muscle damage. The optimal frequency of the micropump device proposed in this study is approximately 40 Hz, which is within the ideal operating frequency range (40–70 Hz) for medical products. According to the relation between the backpressure and the net flow rate shown in Figure 12, it can be seen that the backpressure range of the bio-inspired micropump is approximately 0–5.4 mmHg. Generally, the central venous pressure of the human body falls within 3–9 mmHg. When a patient's central venous pressure decreases due to symptoms such as dehydration or bleeding, the patient must be administered an injection or intravenous drip. For some patients who require the use of chemicals, in addition to a micropump device that is durable and inexpensive, efficient liquid delivery and applicability are necessary. The bio-inspired micropump proposed in this study is widely applicable to central venous drug delivery devices and other industrial applications. Not only can it reduce damage to the human body, but it is also widely applicable to delivery equipment used in many industrial microsystems.

## CONCLUSION

In this paper, the bio-inspired valveless micropump chamber model actuated by a piezo-electric actuator is proposed and constructed by using a two-way fluid-solid coupling system. The research results are summarized as follows:

1. The results of system design and numerical modeling reveal that the bio-inspired valveless micropump chamber does improve upon the system flow efficiency using illustrated bio-inspired micropump system parameters presented in Table 4. The shape of the bio-inspired micropump chamber is designed based on a moving stingray and is featured with smooth streamlines that make the distribution of the internal flow in micropumps concentrated and smoother than the conventional micropump system, and thus reducing the vortex responses inside the bio-inspired chamber of the pump.
2. The results of streamline distribution in chamber indicate that the bio-inspired chamber design does improve on backflow effect and forward moving flow of the fluid. This is because the bio-inspired chamber coupled with membrane deflection of the piezoelectric actuator to strengthen the pressure gradients in the nozzle and diffuser, and thus smoothing out the vortex pattern in operating cycle.
3. Simulation results also indicate that the proposed bio-inspired valveless micropump chamber system induces a higher overall system resonance that dramatically push the system net flow rate to higher level as compared to that of the conventional valveless micropump chamber system. The maximum net flow rate of the proposed bio-inspired micropump is about 1.89 ml/min as the peak voltage is of 100 V and the operating frequency is at 40 Hz. Arriving at system resonant frequency, the net flow rate of the bio-inspired micropump is increased 44% as compared to that of the conventional micropump system. The resonant system frequency of the bio-inspired micropump system is raised up from 31 Hz of the conventional system to about 40 Hz of the bio-inspired system.
4. The proposed bio-inspired device has many advantages such as high flow rate, low cost and high durability, and can be used for efficient delivery of liqueous agents. Not only can it avoid accidental damage to the human body, but it is also widely applicable to efficient delivery equipment of many industrial microsystems. The particular distinct merit of the proposed system is contributed by the backpressure range of the system which turns out to be approximately 0–5.4 mmHg that is very suitable for reliable central venous catheters and automatic drug delivery systems.

## REFERENCES

Whitesides, G.M., 2006. "The origins and the future of microfluidics," *Nature*, 442(7101), 368-373.

Lin, C.H., Hsiao, Y.H., Chang, H.C., Yeh, C.F., He, C.K., Salm, E.M., Chen, C.C., Chiu, I.M., and Hsu, C.H., 2015, "A microfluidic dual-well device for high-throughput single-cell capture and culture," *Lab on a Chip*, 15(14), 2928-2938.

Chin, C.D., Linder, V. and Sia, S.K., 2012, "Commercialization of microfluidic point-of-care diagnostic devices," *Lab on a Chip*, 12(12), 2118-2134.

Dittrich, P.S. and Manz, A., 2006, "Lab-on-a-chip: microfluidics in drug discovery," *Nature reviews Drug discovery*, 5(3), 210-218.

Stemme, E. and Stemme, G., 1993, "A valveless diffuser/nozzle-based fluid pump," *Sensors and Actuators A: physical*, 39(2), 159-167.

Laser, D.J. and Santiago, J.G., 2004, "A review of micropumps," Journal of micromechanics and microengineering, 14(6), R35.

Olsson, A., Stemme, G. and Stemme, E., 1995, "A valve-less planar fluid pump with two pump chambers," Sensors and Actuators A: Physical, *47*(1-3), 549-556.

Gerlach, T. and Wurmus, H., 1995, "Working principle and performance of the dynamic micropump," *Sensors and Actuators A: Physical*, 50(1-2), 135-140.

Koch, M., Harris, N., Evans, A.G., White, N.M. and Brunnschweiler, A., 1998, "A novel micromachined pump based on thick-film piezoelectric actuation," Sensors and Actuators A: Physical, 70, 98-103.

Afrasiab, H., Movahhedy, M.R., and Assempour, A., 2011, "Proposal of a new design for valveless micropumps," Scientia Iranica, 18(6), 1261-1266.

Olsson, A., Stemme, G. and Stemme, E., 2000, "Numerical and experimental studies of flat-walled diffuser elements for valve-less micropumps," Sensors and Actuators A: Physical, 84(1-2), 165-175.

Xu, Y., Yan, W., Cao, T. and Guo, L., 2014, "Study on the valveless micropumps with saw-tooth microchannels," In 11th IEEE International Conference on Control and Automation (ICCA), 1251-1254.

Dich, N.Q., Dinh, T.X., Pham, P.H. and Dau, V.T., 2015, "Study of valveless electromagnetic micropump by volume-of-fluid and OpenFOAM," *Japanese Journal of Applied Physics*, 54(5), 057201.

Singh, S., Kumar, N., George, D. and Sen, A.K., 2015, "Analytical modeling, simulations and experimental studies of a PZT actuated planar valveless PDMS micropump," Sensors and Actuators A: Physical, 225, 81-94.

Lai, H. Y., and Kang, J. H., 2021, “System modeling and characterization of enhanced valveless micropumps,” Mechanics Based Design of Structures and Machines, pp. 1-22.

Timoshenko, S. P. and Woinowsky-Krieger, S., 1959, “*Theory of plates and shells*”, McGraw-Hill.

Jaffe, B., 2012, *Piezoelectric ceramics, (Vol. 3)*, Elsevier.

Li, F., and Li, G., 2015, “Application of ANSYS APDL in the Design of Piezoelectric Transducer,” In 2015 International Conference on Advanced Engineering Materials and Technology. Atlantis Press.

Wang, A.B. and Hsieh, M.C., 2012, “Unveiling the missing transport mechanism inside the valveless micropump,” Lab on a Chip, 12(17), 3024-3027.

Ullmann, A., and Fono, I., 2002, “The piezoelectric valve-less pump-improved dynamic model,” Journal of Microelectromechanical systems, 11(6), 655-664.

# 仿生腔室設計以增強無閥微泵流動效率之研究

賴新一　康景皓
國立成功大學機械工程學系

## 摘要

為了擴大微泵之背壓並增加其淨流量，以達成可適用於高性能工業與醫用微系統之目的,本文提出一套完整理論與和數值建模方法，用以分析設計無閥微泵仿生增強型腔室，並印證該系統流場動力之效能提升。通過與傳統圓形無閥微泵系統的流動力文獻實測數據之比對，證實本文所提之仿生腔室設計方法切實可行。

為了達到設計目標，本文採用了一套雙向流固耦合界面系統（FSIS），提出無閥微泵仿生腔室結構之設計理論與數值建模流程。數值模擬結果表明，當峰值電壓為 100 V，工作頻率約為 40 Hz時，仿生微泵的最大淨流量為 1.89 ml/min，最大背壓為 720 Pa（或 5.4 mmHg），均優於圓形幾何形狀的傳統微泵，且仿生系統之淨流量比諸傳統無圓管微泵值高出了約44%。研究結果還發現仿生無閥微泵的內部流動狀態對系統固有頻率的增加有顯著影響，因為有了更高的共振頻率，故而有效地提升了仿生型微泵的淨流量。